ACS APPLIED MATERIALS & INTERFACES

www.acsami.org

Research Article

Self-Assembly of Impact-Resistant and Shape-Recoverable Structures Inspired by Taiwan Rhinoceros Beetles

Mei-Xuan Wu,[†] Hsiang-Wen Hsueh,[†] Shang-Hsuan Lu, Bo-Han Zeng, Yun-Wen Huang, Cai-Yin Fang, Szu-Yi Yeh, Shih-Hsuan Hsieh, and Hongta Yang*

Cite This: *ACS Appl. Mater. Interfaces* 2025, 17, 24630−24643

Read Online

ACCESS | Metrics & More | Article Recommendations | Supporting Information

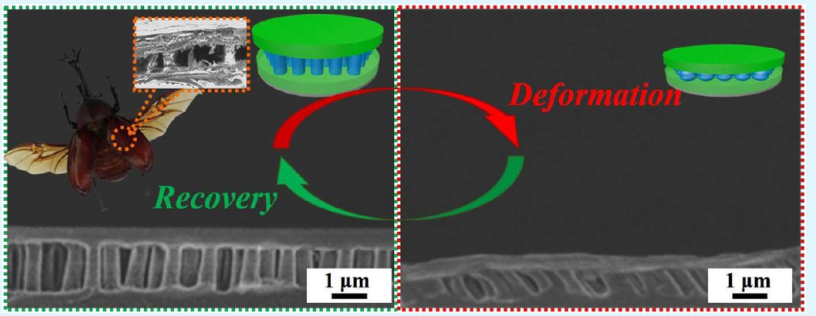

ABSTRACT: Taiwan rhinoceros beetle (*Trypoxylus dichotomus tsunobosonis*) forewings, covered with micrometer-scale sandwich structures, can dissipate impact energies to protect the membranous hindwings underneath. Bioinspired by the forewings, monolayer silica colloidal crystals are self-assembled and utilized as structural templates to engineer sandwich structures, which are supported by nonclose-packed shape memory polymer-based structure arrays. These sandwich structures provide sufficient space for the structural supports to be contorted under external stresses, facilitating the dissipating of impact energies. Importantly, the deformed structures, accompanied by diminished impact resistances, can restore their original states through manipulating the corresponding stimuli-responsive structural transitions under ambient conditions. To gain a better comprehension, the dependences of the structure arrangement, structure size, and structure shape of structural supports on the recoverable impact-resistant capabilities are systematically investigated in this research.

KEYWORDS: *Taiwan rhinoceros beetles, self-assembly, sandwich structures, impact resistance, recoverability*

INTRODUCTION

Recent advances in photolithographic technologies, electronic assembly processes, chip-on-board techniques, and microfluidic systems have provided sufficient support for manufacturing ever-smaller electronic components.[1] The miniaturization of electronic subassemblies can free up space on chips, enabling the development of more compact, portable, and sophisticated electronic devices, optical instruments, military equipment, or medical products, to name just a few.[2−5] Miniaturized devices possess inherent advantages in size/weight reductions, higher operating speeds, and less power consumption; nevertheless, there is a difficulty in material selection for encasement design and production. While melt-processable, lightweight, and affordable, polymer-based materials utilized for thin-wall encasements experience a considerable loss of mechanical strength, which greatly increases the risk of failure under external loads.[6] To tackle this problem, various alloys have been invented to replace plastic encasements for enhancing mechanical behaviors.[7,8] Unfortunately, these alloys inevitably suffer from low design freedom, high density, and costliness. Therefore, designing and building casing materials for practical applications remains challenging.

In the past few years, porous coatings with a whole range of pore sizes and geometries have been applied to dissipate impact energies.[9−12] Compared with the physical properties of bulk materials, these porous structures possess lower densities and degraded mechanical strengths, making them deform more easily under external loads. The resulting structural deformations further conduce to enhanced impact energy dissipations. However, most cellular structures, produced using either physical or chemical foaming agents, are limited by inefficient distributions of cells.[13,14] The stochastic processing of structures categorically brings about an uneven impact-resistant capability.

Received: February 24, 2025
Revised: April 7, 2025
Accepted: April 7, 2025
Published: April 10, 2025

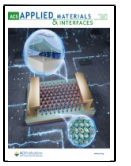

https://doi.org/10.1021/acsami.5c03894
ACS Appl. Mater. Interfaces 2025, 17, 24630−24643

Moreover, the damaged structures cannot be recovered, which severely restricts their long-term durability.

Over 570 million years of evolution and natural selection, living organisms have adopted diverse strategies to improve their survival chances. Taking leaf beetles, gold beetles, weevils, ladybugs, stag beetles, and unicorn beetles as examples, their forewings are specialized into hard sheaths, also known as elytra, to protect hindwings and bodies from being attacked by birds or lizards.[15−20] Intriguingly, the elytra of male Taiwan rhinoceros beetles exhibit particularly excellent impact resistances, even allowing the beetles to fight with each other during mating battles or food competitions.[21] Recent studies have found that these elytra are covered with hollow sandwich structures, which are formed from groupings of sheet-like upper/lower laminates and nonclose-packed trabeculae in between.[22,23] The trabeculae are micrometer-scale tissue elements in the form of pillar-shaped beams, which can be deformed to absorb impact energies when the sandwich structures are subjected to external stresses. As a result, the presence of sandwich structures makes the elytra lightweight, and offers better protection than those of solid structures. Importantly, these deformed natural structures can be gradually recovered with time.

Bioinspired by the Coleoptera insects, a wide spectrum of artificial impact-resistant materials, such as hollow bricks, have been manufactured and applied in our daily lives.[24,25] Despite that, the design and fabrication of micrometer-scale hollow sandwich structures are seldom reported. Fueled by the appreciable advancements in lithography-based technologies, numerous colloidal lithographic methodologies have been developed to pattern high-resolution microstructure arrays.[26−28] In the patterning processes, monodispersed colloidal particles are self-assembled to form two-dimensional (2D) colloidal crystals, and then serve as etching masks to construct demanded features onto selected substrates through adjusting the etching parameters. These well-arranged micrometer-scale features can be envisaged as a stepping-stone for organizing hollow sandwich structures. Unfortunately, most existing colloidal self-assembly approaches, including evaporation-induced self-assembly, interface-induced self-assembly, template-assisted methods, external physical fields-induced self-assembly, and chemical stimuli-induced self-assembly, are not feasible with standard microfabrication processes.[29−33] Apart from that, these bottom-up fabrication methodologies can only bring about close-packed colloidal crystals, whereas nonclose-packed arrangements of colloidal particles are desired for mimicking those natural structures on the elytra. Benefiting from the swift progress of self-assembly technologies, a microfabrication-compatible approach is innovated to deposit nonclose-packed colloidal templates in a single spin-coat step.[34,35] The structural templates can be exploited to generate pillar-shaped artificial trabeculae with more interstructure space, which constitutes a framework for creating hollow sandwich structures. Nevertheless, the requirement of recoverable impact-resistant abilities for the bioinspired sandwich structures is another inherent concern that must be resolved.

The discovery of shape memory polymers, capable of reversibly converting their molecular configurations in response to external stimuli, offers a promising solution to address this issue. The application of physical or chemical stimuli, such as heat, ultraviolet radiations, lasers, magnetic/electric fields, chemical solvents, and so on, can enhance the molecular chain mobilities of shape memory polymers, which further trigger their entropy-driven elastic recoveries.[36−39] As a result, distorted shape memory polymer-based structural features are able to restore their original shapes on demand. Although most existing stimuli-responsive polymers have high shape deformability and reliable manufacturability, the physical stimuli-responsive structural recoveries take time and patience, considerably hindering their practical uses that require rapid responses. In comparison, chemical stimuli-responsive ones take much less time. However, the adoption of specific chemicals inevitably causes adverse damage to other device components, or even incurs detrimental environmental issues.[40] Moreover, these structural transitions of reconfigurable features still experience limitations with short-term operations. Therefore, a new type of structural recovery mechanism is highly demanded.

Herein, a room-temperature shape memory polymer is devised and applied to engineer Taiwan rhinoceros beetle-inspired hollow sandwich structures. The sandwich structures are directly patterned onto selected substrates by combining a shear force-induced colloidal self-assembly technology with a colloidal lithographic method. In contrast to traditional shape memory polymer-based structures, these as-fabricated structures can swiftly convert their configurations by regulating the evaporation of common solvents, such as ethanol, water, toluene, or acetone, under ambient conditions. The interdisciplinary integration of room-temperature shape memory polymers and hollow sandwich structures delivers an uncomplicated strategy to realize recoverable impact-resistant capabilities. Instead of tensile tests or dynamic thermomechanical analyses, nanoindentation tests are employed to investigate micrometer-scale impact-resistant enhancements of the bioinspired structures.[41] In this research, the mechanical characteristics of disparate sandwich structures are evaluated to guide an optimum structural design for miniaturized device applications.

EXPERIMENTAL SECTION

Materials. Taiwan rhinoceros beetle specimens, which have been selected a bioinspired prototype, are collected from the Muh-Sheng Museum of Entomology. Monodispersed silica spheres, with a diameter standard deviation of less than 5%, are prepared according to the well-established StÖber synthetic process.[42] All the chemicals and solvents, including tetraethyl orthosilicate (Merck KGaA), ammonium hydroxide (Merck KGaA), anhydrous ethanol (Echo Chemical), and deionized water (18.2 MΩ·cm, Millipore) are of reagent quality. Photocurable SR415 ethoxylated trimethylolpropane triacrylate oligomers (ETPTA, Sartomer), photocurable SR610 ethylene glycol diacrylate oligomers (EGDA, Sartomer), and Darocur 1173 2-hydroxy-2-methyl-1-phenyl-1-propanone (HMPP, BASF), as a photoinitiator, are utilized without any further purification. A diluted hydrofluoric acid aqueous solution (HF, Merck KGaA) is applied as a silica-etching agent. Two-part Sylgard 184 poly(dimethylsiloxane) (PDMS) elastomer kits are obtained from Dow Corning. Commercial microscope cover glass (0.13−0.16 mm in thickness, Corning) is rinsed with deionized water before use.

Self-Assembly of a Non-Close-Packed Colloidal Monolayer of Silica Spheres. The StÖber silica spheres are cleansed using anhydrous ethanol through 5 dispersion/centrifugation cycles, followed by redispersing the silica spheres in a mixture of SR415 ETPTA oligomers and Darocur 1173 HMPP with the use of a UP100H probe-type ultrasonic homogenizer (Hielscher Ultrasonics). The volume ratios of silica spheres, ETPTA oligomers, and HMPP are adjusted to be 20:79:1. After filtrating through a nylon syringe filter with an average pore size of 2.0 μm (Whatman) to eliminate aggregated silica spheres, the silica suspension is deposited and spread onto a cover glass, which has been coated with PETPTA/PEGDA layers. The cover glass is then spun at 200 rpm for 1 min, 400 rpm for 1 min, 800 rpm for 0.5 min, 2000 rpm for 0.5 min, 4000 rpm for 0.5 min, and 6000 rpm for 4.5 min, progressively, utilizing a WS-650−23B spin-coater (Laurell Technol-

https://doi.org/10.1021/acsami.5c03894
ACS Appl. Mater. Interfaces 2025, 17, 24630−24643

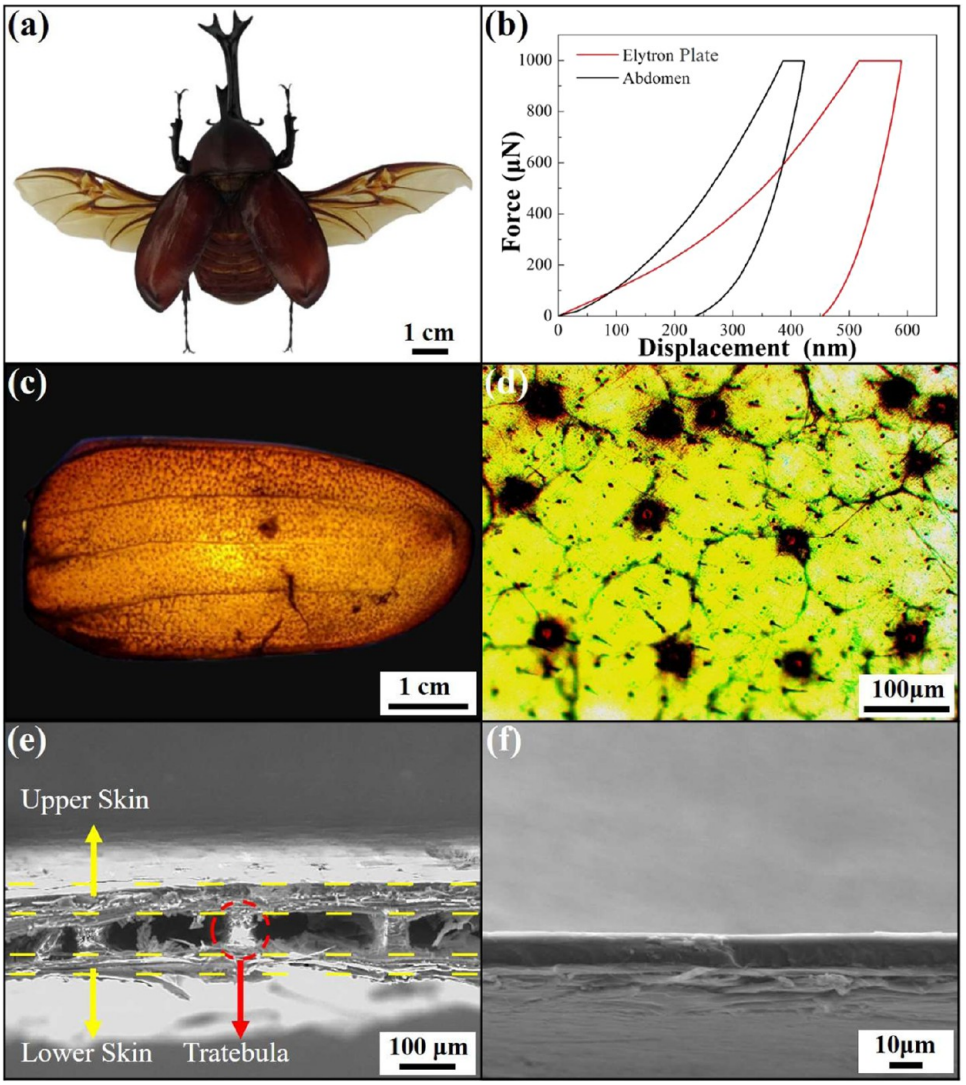

Figure 1. (a) Photograph of a Taiwan rhinoceros beetle taken under natural light illumination. (b) Load−displacement curves with maximum loads of 1000 μN for the elytron plate (red curve) and abdomen (black curve) of this Taiwan rhinoceros beetle. (c) Photograph, (d) optical micrograph, and (e) cross-sectional SEM image of the beetle elytron plates. (f) Cross-sectional SEM image of the beetle abdomen.

ogies).[43,44] In the spin-coating process, the silica spheres are shear-aligned into a two-dimensionally nonclose-packed arrangement. The oligomers are subsequently photopolymerized for 0.5 min in a high-powered LED UV-curing oven (CureUV).

Templating Fabrication of Non-Close-Packed Structure Arrays. The self-assembled silica colloid crystals can further serve as structural templates during an argon/oxygen reactive ion etching (Ar/O_2 RIE) process, operating on a PlasmaPro 100 Polaris inductively coupled plasma reactive ion etching system (Oxford Instruments). In the plasma etching process, the power density and chamber pressure are kept at 75 W and 20 mTorr, respectively, while the gas flow rates vary from 0 to 40 SCCM. The templating silica spheres are finally removed by rinsing with a diluted HF aqueous solution (1 vol %) to pattern nonclose-packed structure arrays on the glass substrate directly.

Engineering of Taiwan Rhinoceros Beetle-Inspired Impact-Resistant Structures. Sylgard 184 silicone elastomer base and curing agent are mixed at a weight ratio of 15:1 using an ultrasonic homogenizer, and then transferred into a Nalgene vacuum chamber (Thermo Scientific) for 30 min to eliminate trapped air bubbles. The degassed mixture is subsequently poured into a Brand Petri dish (10.0 cm in diameter, Merck KGaA), of which a piece of ultrathin PET film with a size of 5.0 × 5.0 cm^2 (0.5 μm in thickness, Dadao Packing Materials) is placed on the bottom. After being cured under ambient conditions for 24 h, the solidified PDMS film is gently peeled off and used as a dish with depth on demand. The PDMS dish can be filled with an ETPTA oligomer/EGDA oligomer/HMPP mixture, followed by a spin-coating process operating at 100 rpm for 5 min to remove any excess mixture. Afterward, the aforementioned nonclose-packed structure array is dipped into the oligomer mixture, which is then photopolymerized on exposure to UV radiation for 10 s. The as-engineered structures are finally peeled off from the PDMS dish to bring about bioinspired impact-resistant structures.

Characterization. A Lumix DMC-FZ300 digital camera (Panasonic), an OBS106 transmitted light microscope (Kern), and a JSM-IT710HR Schottky field emission scanning electron microscope (JEOL) are utilized to collect photographs, optical micrographs, and scanning electron microscopy (SEM) images of the samples, respectively. Prior to the SEM imaging, a platinum layer is sputtered onto the samples using an AGB7366 manual sputter coater (Agar Scientific). Mechanical behaviors of the samples are investigated by a TI980 Tribo-Indenter test system (Hysitron) equipped with a standard Berkovich tip. The measurements of each sample are repeated 10 times under ambient conditions, and the average values are reported.

RESULTS AND DISCUSSION

Taiwan rhinoceros beetles (*Trypoxylus dichotomus tsunobosonis*) are characterized by a pair of toughened forewings, which are

https://doi.org/10.1021/acsami.5c03894
ACS Appl. Mater. Interfaces 2025, 17, 24630−24643

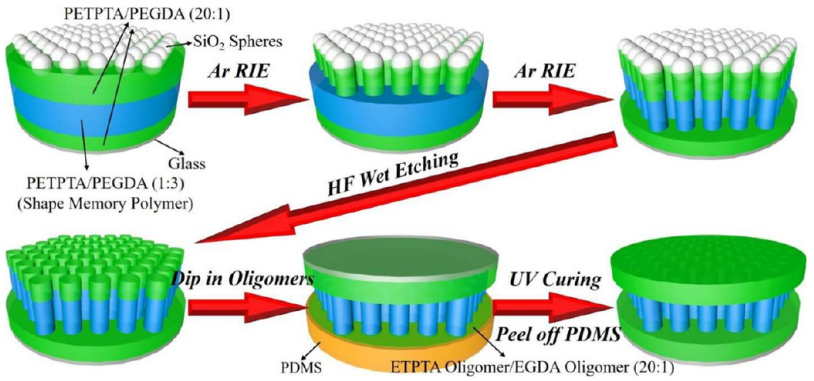

Figure 2. Schematic illustration of the templating procedures for engineering Taiwan rhinoceros beetle-inspired impact-resistant structures on glass substrates.

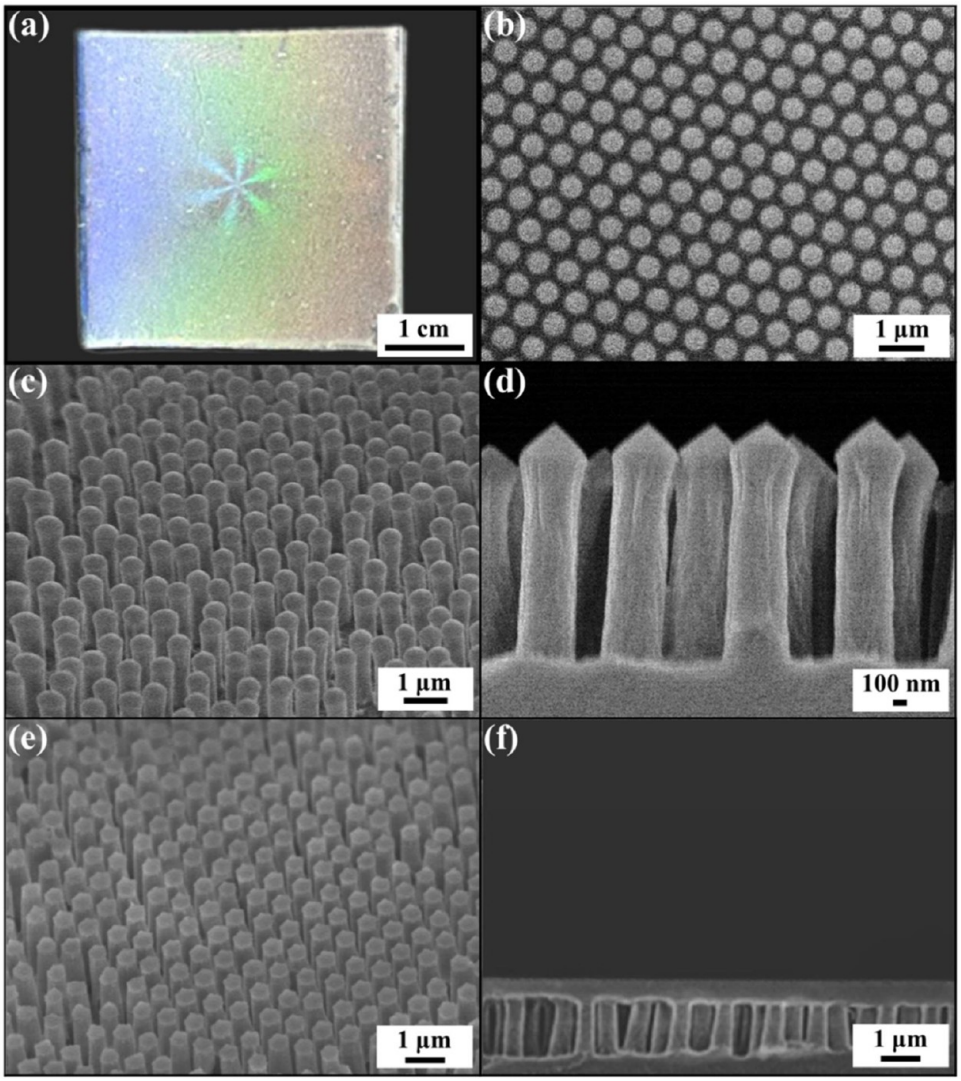

Figure 3. (a) Photograph of a glass substrate, which is sequentially spin-coated with a PETPTA/PEGDA (20:1) layer, a PETPTA/PEGDA (1:3) layer, a PETPTA/PEGDA (20:1) layer, and a nonclose-packed colloidal monolayer of 500 nm silica spheres. The thickness ratio of each polymer layer is adjusted to be 1:2:1, while the average interparticle distance is controlled to be 1.4 *D*, where *D* denotes the diameter of silica spheres. (b) Top-view SEM image of the sample in (a). (c) Tilted-view SEM image and (d) magnified cross-sectional SEM image of the king oyster mushroom-like structure array templated from the silica colloidal crystals by reactive ion etching (Ar (40 SCCM)). (e) Tilted-view SEM image of the corresponding column-shaped structure array. (f) Cross-sectional SEM image of the as-fabricated impact-resistant structures.

known as elytra (Figure 1 (a)). The beetle elytron plates can withstand external loadings and dissipate impact energies to protect the membranous hindwings, thorax, and abdomen underneath. To acquire a more profound understanding, the

https://doi.org/10.1021/acsami.5c03894
ACS Appl. Mater. Interfaces 2025, 17, 24630−24643

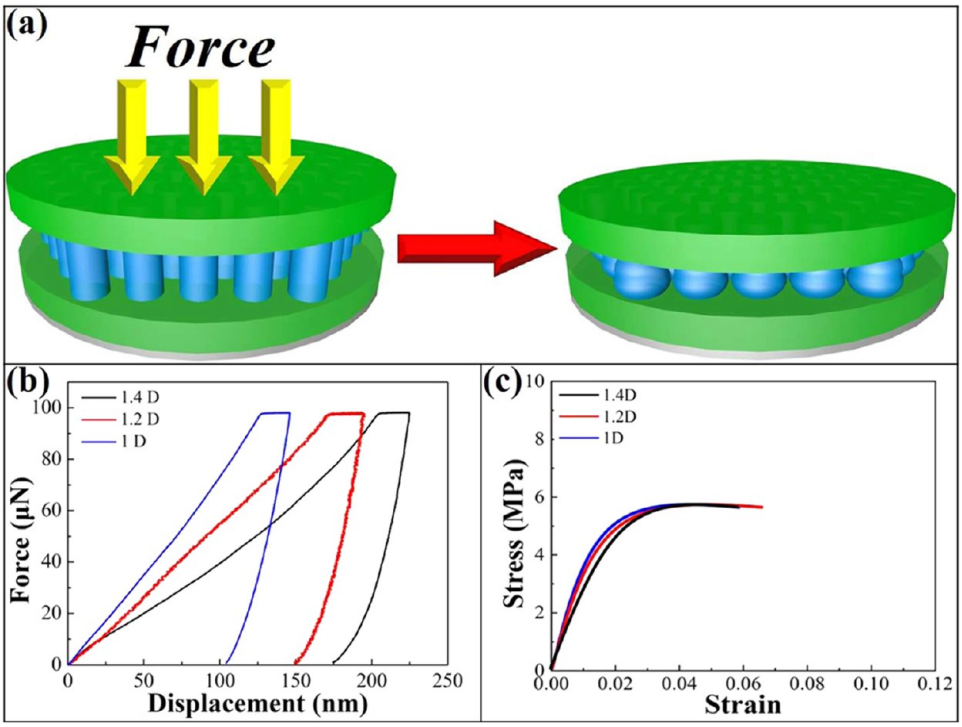

Figure 4. (a) Schematic illustration of the force applied onto the Taiwan rhinoceros beetle-inspired impact-resistant structure. (b) Load−displacement curves with maximum loads of 100 μN and (c) the corresponding indentation stress-indentation strain curves for the bioinspired impact-resistant structures. The interstructure distances are controlled to be 1.4 D (black curve), 1.2 D (red curve), and 1 D (blue curve), respectively, where D denotes the diameter of silica spheres (500 nm).

mechanical properties of the elytra and abdomen are investigated through nanoindentation tests under maximum loads of 1000 μN (Figure 1 (b)). On the assumption of negligible adhesion, their Young's moduli (E) and indentation hardnesses (H) can be determined directly from nanoindentation analyses using the Oliver-Pharr model, of which $E = \frac{S\sqrt{\pi}}{2\sqrt{A}}$ and $H = \frac{F_{max}}{A}$.[45,46] In the relationships, S refers to the slope of the unloading curve at the maximum load (F_{max}), while A denotes the projected contact area between the nanoindenter tip and the beetle specimen. Besides that, the enclosed area of each load−displacement curve represents their corresponding dissipation impact energies.[47] As summarized in Table S1, the Young's modulus and indentation hardness of the abdomen are calculated as 7.01 ± 0.33 and 0.31 ± 0.03 GPa, respectively, which agree well with the findings have been reported in previous researches.[48,49] In comparison, the elytra are with a lower Young's modulus (4.38 ± 0.74 GPa) and a lower indentation hardness (0.15 ± 0.05 GPa). The reductions in the mechanical behaviors are derived from the presence of air within the elytra. As evidenced in Figure 1 (c)−(e), the beetle elytron plates consist of an upper laminate (*ca.* 47 μm in thickness) and a lower laminate (*ca.* 43 μm in thickness), which are connected through randomly arranged trabeculae (*ca.* 83 μm in height). These sandwich structures not only allow air to be occupied between the laminates to make the beetle forewings lightweight, but also provide enough space to facilitate the temporary deformation of trabeculae under external stresses. Accordingly, impact energies can be dissipated more efficiently on the sandwich structures (0.21 ± 0.02 nJ) than the solid ones (Figure 1(f)) (0.09 ± 0.01 nJ), even though both of them are composed of protein and chitin fibers.

Bioinspired by the impact-resistant characteristics of Taiwan rhinoceros beetle forewings, sandwich structures are engineered using a colloidal lithographic approach (Figure 2). In the fabrication procedures, a glass substrate is sequentially spin-coated with a PETPTA/PEGDA (20:1 vol/vol) layer, a PETPTA/PEGDA (1:3 vol/vol) layer, and a PETPTA/PEGDA (20:1 vol/vol) layer, followed by another spin-coating process to shear-align a nonclose-packed silica colloidal monolayer onto the PETPTA/PEGDA layers. The self-assembled silica spheres can be utilized as structural templates to pattern the top two PETPTA/PEGDA layers in a plasma etching process. Afterward, the silica templates are wet-etched by HF to develop column-shaped structures on the bottom PETPTA/PEGDA layer. The structure array is then dipped into an ETPTA oligomer/EGDA oligomer/HMPP mixture, which has been deposited on a homemade PDMS dish before use. In this oligomer mixture, the volume ratio of ETPTA oligomers to EGDA oligomers is controlled to be 20:1. After photopolymerization of the oligomers, the as-fabricated sandwich structures can be peeled off from the PDMS dish easily. It is worth mentioning that the thickness of each PETPTA/PEGDA layer and the arrangement of silica spheres can be manipulated by modifying the spin-coating parameters.[50,51] In view of this, it is feasible to design and build Taiwan rhinoceros beetle-inspired impact-resistant structures with varied configurations.

Acquiring knowledge from the beetle elytron plates, the thickness ratio of each PETPTA/PEGDA layer is adjusted to be 1:2:1. Here, a cover glass is spin-coated with a 500 nm-thick PETPTA/PEGDA (20:1) layer, a 1 μm-thick PETPTA/PEGDA (1:3) layer, and a 500 nm-thick PETPTA/PEGDA (20:1) layer in succession (Figure S1). Subsequently, a colloidal monolayer of 500 nm silica spheres is shear-aligned onto the PETPTA/PEGDA layers. As shown in Figure 3(a), the self-

https://doi.org/10.1021/acsami.5c03894
ACS Appl. Mater. Interfaces 2025, 17, 24630−24643

Table 1. Values of Young's Modulus, Hardness, and Dissipation Energy for the Taiwan Rhinoceros Beetle-Inspired Impact-Resistant Structures[a]

Sample	Porosity	Experimental / Theorical Young's Modulus (GPa)	Hardness (GPa)	Dissipation Energy (10^{-12} J)
1.4 D 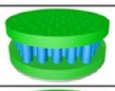	0.27	2.50 ± 0.22 / 2.62	0.08 ± 0.01	9.31 ± 0.15
1.2 D 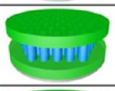	0.18	2.84 ± 0.09 / 2.92	0.08 ± 0.01	8.04 ± 0.63
1 D 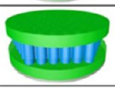	0.04	3.17 ± 0.16 / 3.41	0.09 ± 0.01	6.59 ± 0.47

[a]The inter-structure distances are controlled to be 1.4 *D*, 1.2 *D*, and 1 *D*, respectively, where D denotes the diameter of silica spheres (500 nm).

assembled silica colloidal crystals exhibit a characteristic six-arm diffraction pattern under natural lighting, identifying the presence of hexagonally nonclose-packed arrangement of silica spheres across the whole glass substrate (Figure 3(b)).[51] It is worthy to note that the average intersphere distance equals 1.4 *D*, where *D* denotes the diameter of silica spheres. Owing to the high RIE selectivity of polymers against silica, the silica spheres can serve as lithographic masks to protect the PETPTA/PEGDA copolymers underneath them from being etched by Ar reactive ions. After patterning the top two PETPTA/PEGDA layers, king oyster mushroom-like structures, consisting of silica tops, PETPTA/PEGDA (20:1) middles, and PETPTA/PEGDA (1:3) bottoms, are generated on the PETPTA/PEGDA (20:1) layer-coated glass substrate (Figure 3(c),(d)). The remaining silica tops are then wet-etched to create column-shaped polymeric structures (Figure 3(e)). Apparently, their long-range hexagonal arrangement and interstructure distances are well-preserved during the templating procedures. The column-shaped structure array can further be applied as structural supports to construct sandwich structures. It appears that the as-engineered structures are comprised of a PETPTA/PEGDA (20:1) upper layer (*ca.* 500 nm in thickness) and a PETPTA/PEGDA (20:1) lower layer (*ca.* 500 nm in thickness), which are connected through hexagonally arranged PETPTA/PEGDA (1:3) column-shaped structures (*ca.* 1 μm in height) (Figure 3(f)). In addition, the average distance between the column-shaped structures is approximately equal to 1.4 *D*. As predicted, the sandwich structures with varied interstructure distances of 1.2 *D* and 1.0 *D* can be developed as well through manipulating the arrangement of silica templates (Figures S2, S3, and S4).

To assess the dependence of structural configuration on mechanical properties, load−displacement curves of the aforementioned featureless PETPTA/PEGDA coating layers and Taiwan rhinoceros beetle-inspired sandwich structures are performed under maximum indentation loads of 100 μN that are directed in the normal direction (Figure 4(a)). As shown in Figure S5 and Table S2, either triple-layer or single-layer PETPTA/PEGDA coatings behave with similar Young's moduli (~3.58 GPa), indentation hardnesses (~0.09 GPa), and dissipation energies (~5.99 pJ). These characterized values match well with previous studies.[52,53] By comparison, lower Young's moduli and indentation hardnesses are found on the bioinspired sandwich structures (Figure 4(b) and Table 1). Besides that, the Young's modulus of the sandwich structure is decreased from 3.17 ± 0.16 to 2.50 ± 0.22 GPa as the average distance between the column-shaped structures increases from 1.0 *D* to 1.4 *D*, while the corresponding indentation hardness gradually decreases from 0.09 ± 0.01 to 0.08 ± 0.01 GPa with the increase of interstructure distance. It is evidenced that the formation of larger space within the sandwich structures brings about even lower mechanical behaviors. These load−displacement curves in these loading/unloading cycles can further convert into indentation stress-indentation strain curves following the Hertz's theory (Figure 4(c)).[54] The initial slopes of each stress−strain curve represent their corresponding Young's moduli. Clearly, the characterized Young's modulus is decreased with the increase of average distance between the column-shaped structures, which is consistent with the above-mentioned results. Moreover, the reduction in the Young's modulus are theoretically expounded using the following relation proposed by Phani and Niyogi's groups.[55,56]

$$E = E_0 \times (1 - \varphi)$$

In this relation, E indicates the Young's modulus of a structured material with a porosity of φ, and E_0 represents the Young's modulus of the pore-free material. The φ is defined as $\frac{V_v}{V_B}$, in which V_v is the void volume, and V_B is the bulk volume of the structured material. As illustrated in Figure S6, the V_v and V_B per volume element of the bioinspired sandwich structures are given by

$$V_v = \left[\frac{\left(\frac{\sqrt{3}d}{2}\right) \times d}{2} - \frac{\pi \times \left(\frac{D}{2}\right)^2}{2} \right] \times h_{column}$$

$$V_B = \frac{\left(\frac{\sqrt{3}d}{2}\right) \times d}{2} \times (T_{upper} + h_{column} + T_{lower})$$

where d, T_{upper}, h_{column}, and T_{lower} denote the interstructure distance, the thickness of the upper layer (500 nm), the height of column-shaped structures (1 μm), and the thickness of the lower layer (500 nm), respectively. On that account, an increase in the interstructure distance (d) creates a larger porosity (φ), and thus leads to a reduced Young's modulus (E). As verified in Table 1, the estimated porosity increases from 0.04 to 0.27 as the interstructure distance varies from 1.0 *D* to 1.4 *D*, while the theoretical Young's modulus decreases from 3.41 to 2.62 GPa. It is worthy to mention that these theoretical values are greater than the experimental ones, though both of them exhibit similar tendencies in their reductions of Young's moduli. This distinguishable discrepancy is attributed to the presence of nonuniformly distributed interspaces within the sandwich

https://doi.org/10.1021/acsami.5c03894
ACS Appl. Mater. Interfaces 2025, 17, 24630−24643

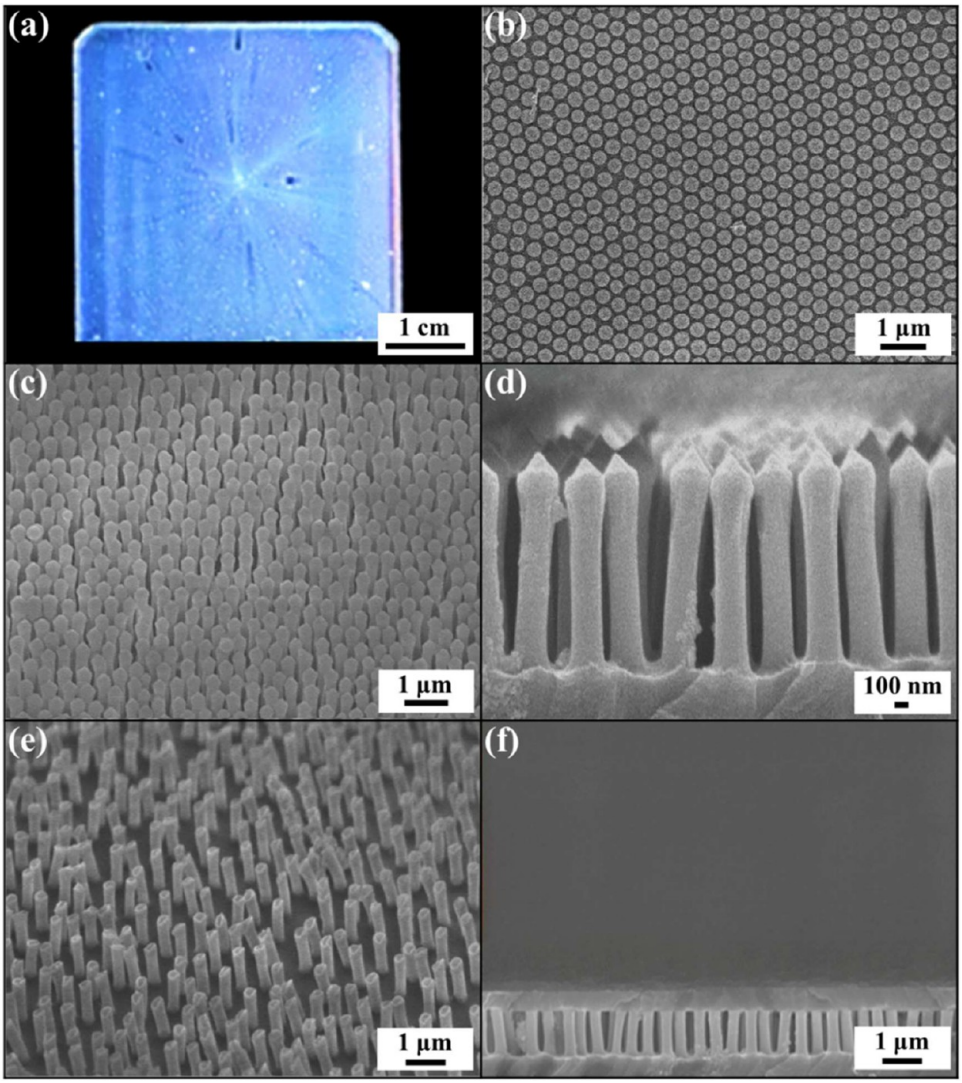

Figure 5. (a) Photograph of a glass substrate, which is sequentially spin-coated with a PETPTA/PEGDA (20:1) layer, a PETPTA/PEGDA (1:3) layer, a PETPTA/PEGDA (1:3) layer, and a nonclose-packed colloidal monolayer of 300 nm silica spheres. The average interparticle distance is controlled to be 1.4 *D*, where *D* denotes the diameter of silica spheres. (b) Top-view SEM image of the sample in (a). (c) Tilted-view SEM image and (d) magnified cross-sectional SEM image of the king oyster mushroom-like structure array templated from the silica colloidal crystals by reactive ion etching (Ar (40 SCCM)). (e) Tilted-view SEM image of the corresponding column-shaped structure array. (f) Cross-sectional SEM image of the as-fabricated impact-resistant structures.

Table 2. Values of Young's Modulus, Hardness, and Dissipation Energy for the Taiwan Rhinoceros Beetle-Inspired Impact-Resistant Structures Templated from Non-Close-Packed 500 nm Silica Colloidal Crystals and Non-Close-Packed 300 nm Silica Colloidal Crystals, Respectively[a]

Sample	Porosity	Experimental / Theorical Young's Modulus (GPa)	Hardness (GPa)	Dissipation Energy (10^{-12} J)
1.4 *D* (500 nm) 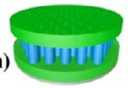	0.27	2.50 ± 0.22 / 2.62	0.08 ± 0.01	9.31 ± 0.15
1.4 *D* (300 nm) 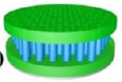	0.27	2.09 ± 0.02 / 2.62	0.07 ± 0.01	9.78 ± 0.36

[a]The inter-structure distances are adjusted to be 1.4 *D*, where *D* denotes the diameter of silica spheres.

structures. Crucially, the reduced Young's modulus accompanying the increased interstructure distance facilitates the deformation of column-shaped structures under external stresses. This further generates a larger projected contact area between the nanoindenter tip and the sandwich structure in a nanoindentation analysis. The resulting indentation hardness

https://doi.org/10.1021/acsami.5c03894
ACS Appl. Mater. Interfaces 2025, 17, 24630−24643

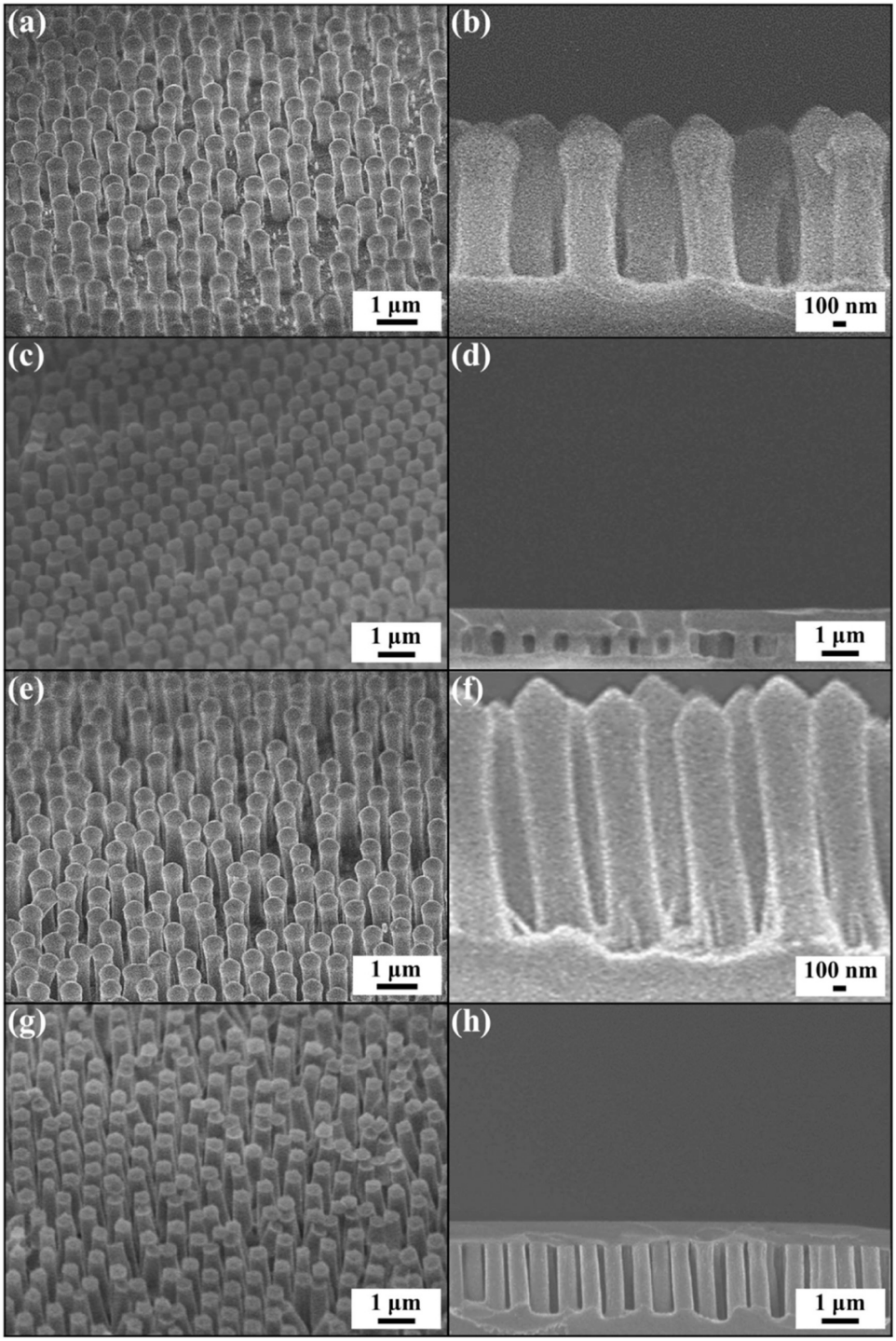

Figure 6. (a) Tilted-view SEM image and (b) magnified cross-sectional SEM image of the king oyster mushroom-like structure array templated from a nonclose-packed colloidal monolayer of 500 nm silica spheres by reactive ion etching (Ar (40 SCCM)). The thickness ratio of each polymer layer is adjusted to be 1:1:1, while the average interparticle distance is controlled to be 1.4 *D*, where *D* denotes the diameter of silica spheres. (c) Tilted-view SEM image of the corresponding column-shaped structure array. (d) Cross-sectional SEM image of the as-fabricated impact-resistant structures. (e) Tilted-view SEM image and (f) magnified cross-sectional SEM image of the king oyster mushroom-like structure array templated from the nonclose-packed silica colloidal crystals by reactive ion etching (Ar (40 SCCM)). The thickness ratio of each polymer layer is adjusted to be 1:3:1. (g) Tilted-view SEM image of the corresponding column-shaped structure array. (h) Cross-sectional SEM image of the as-fabricated impact-resistant structures.

$\left(H = \frac{F_{max}}{A}\right)$, therefore, decreases with the increase of interstructure distance.[45] By contrast, the corresponding dissipation energy is increased from 6.59 ± 0.47 to 9.31 ± 0.15 pJ as the interstructure distance varies from 1.0 *D* to 1.4 *D*. Most of all, the amount of dissipation energy can even be increased by approximate 55.4%, in comparison with that of a triple-layer PETPTA/PEGDA coating. The results disclose that the introduction of larger porosity brings in a reduced Young's modulus, and allows the sandwich structures to dissipate impact energies more efficiently.

https://doi.org/10.1021/acsami.5c03894
ACS Appl. Mater. Interfaces 2025, 17, 24630−24643

Table 3. Values of Young's Modulus, Hardness, and Dissipation Energy for the Taiwan Rhinoceros Beetle-Inspired Impact-Resistant Structures with Varied Polymer Layer Thickness Ratios[a]

Sample	Porosity	Experimental / Theorical Young's Modulus (GPa)	Hardness (GPa)	Dissipation Energy (10^{-12} J)
ETPTA/SMP/ETPTA (1:1:1) 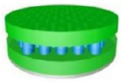	0.18	2.93 ± 0.13 / 2.94	0.09 ± 0.01	7.0 ± 0.44
ETPTA/SMP/ETPTA (1:2:1) 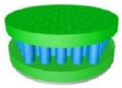	0.27	2.50 ± 0.22 / 2.62	0.08 ± 0.01	9.31 ± 0.15
ETPTA/SMP/ETPTA (1:3:1) 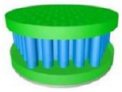	0.40	1.93 ± 0.22 / 2.14	0.06 ± 0.01	10.18 ± 0.88

[a]The inter-structure distances are adjusted to be 1.4 D, where D denotes the diameter of silica spheres (500 nm).

The structural geometry effect on the impact-resistant capability is also investigated in this research. Instead of 500 nm silica spheres, 300 nm silica spheres are shear-aligned into a nonclose-packed arrangement, and then utilized as structural templates to build a bioinspired sandwich structure (Figures S7 and 5). The as-constructed sandwich structure consists of a 500 nm-thick PETPTA/PEGDA (20:1) upper layer, hexagonally arranged 1 μm-high PETPTA/PEGDA (1:3) column-shaped structures, and a 500 nm-thick PETPTA/PEGDA (20:1) lower layer. Noteworthily, the average distance between the column-shaped structures is found to be 1.4 D, where D equals 300 nm. Compared with the mechanical behaviors of the sandwich structure templated from 500 nm silica colloidal crystals (1.4 D), it is explicit that the one templated from 300 nm silica colloidal crystals (1.4 D) exhibits a lower Young's modulus (2.09 ± 0.02 GPa) and a decreased indentation hardness (0.07 ± 0.01 GPa) under a maximum indentation load of 100 μN (Figure S8 and Table 2). In spite of the fact that both of the sandwich structures have the same porosity of 0.27, the one supported by slenderer column-shaped structures can be contorted more easily. As a result, more impact energy (9.78 ± 0.36 pJ) is dissipated once a stress is applied onto this structure. The mechanical behaviors of Taiwan rhinoceros beetle-inspired sandwich structures with varied heights of column-shaped structural supports are evaluated as well (Figure S9). These structural supports are templated from nonclose-packed 500 nm silica colloidal monolayers (1.4 D) using Ar reactive ions (40 SCCM) for different RIE durations. It is evidenced that the application of longer anisotropic RIE treatments results in the constitution of higher column-shaped structural supports (Figure 6). Perspicuously, all of the as-fabricated sandwich structures comprise a 500 nm-thick PETPTA/PEGDA (20:1) upper layer and a 500 nm-thick PETPTA/PEGDA (20:1) lower layer, while the height of their structural supports is varied from 500 nm to 1.5 μm. Accordingly, the thickness ratio of each structural layer is adjusted to be 1:1:1, 1:2:1 (Figure 3), and 1:3:1, respectively. As anticipated, the presence of higher structural supports creates a larger porosity within the sandwich structures, and hence provides more space to dissipate impact energies (Figure S10 and Table 3). The resulting dissipation energy can therefore be increased from 7.00 ± 0.44 (1:1:1), to 9.31 ± 0.15 (1:2:1), to 10.18 ± 0.88 pJ (1:3:1).

To gain a deeper understanding, sandwich structures with different shapes of structural supports have been developed (Figure S11(a)). In addition to the column-shaped structure array, frustum-shaped and cone-shaped structure arrays are fabricated using the nonclose-packed 500 nm silica colloidal crystals (1.4 D) as lithographic masks, while the etching gas (Ar/O_2) flow rates are varied from 10 SCCM/15 SCCM to 10 SCCM/30 SCCM. In the colloidal lithography process, the integration of anisotropic Ar RIE and isotropic O_2 RIE leads to the formation of king oyster mushroom-like structures, consisting of spherical silica caps and frustum-shaped PETPTA/PEGDA stems (Figure 7). Importantly, the application of a higher O_2 flow rate makes the stems become even sharper, primarily owing to the enhancement of isotropic etching. On account of this, hexagonally arranged frustum-shaped and cone-shaped structures can be realized after wet-etching the silica caps. These structure arrays are subsequently employed as structural supports to erect sandwich structures following the above-mentioned fabrication procedures. It is worth noting that the tops of these structures are embedded within the upper layers of the sandwich structures, and thus create frustum-shaped structural supports (Figure S9(b)). Apparently, the average top diameter (~200 nm) of the structural supports templated from the cone-shaped structure array is smaller than that (~350 nm) templated from the frustum-shaped structure array, whereas either of them has an average base diameter of 500 nm. The sandwich structure supported by the sharper structure array renders a larger porosity (0.35), which brings about an even lower Young's modulus (1.50 ± 0.14 GPa) and a decreased indentation hardness (0.06 ± 0.01 GPa) (Figure S12 and Table 4). Crucially, these sharper structures can be contorted more severely in response to external stresses. The employment of sharp structural supports, therefore, facilitates the structural deformation of sandwich structures, and allows impact energies (12.71 ± 1.04 pJ) to be dissipated more effectively (Figure S13).

Load−displacement curves with maximum loads of 100 and 500 μN for a triple-layer PETPTA/PEGDA coating and a Taiwan rhinoceros beetle-inspired sandwich structure are further compared in Figure S14 to ascertain the effect of the applied load on the impact resistance of sandwich structures. Here, the thickness of each triple-layer PETPTA/PEGDA

https://doi.org/10.1021/acsami.5c03894
ACS Appl. Mater. Interfaces 2025, 17, 24630−24643

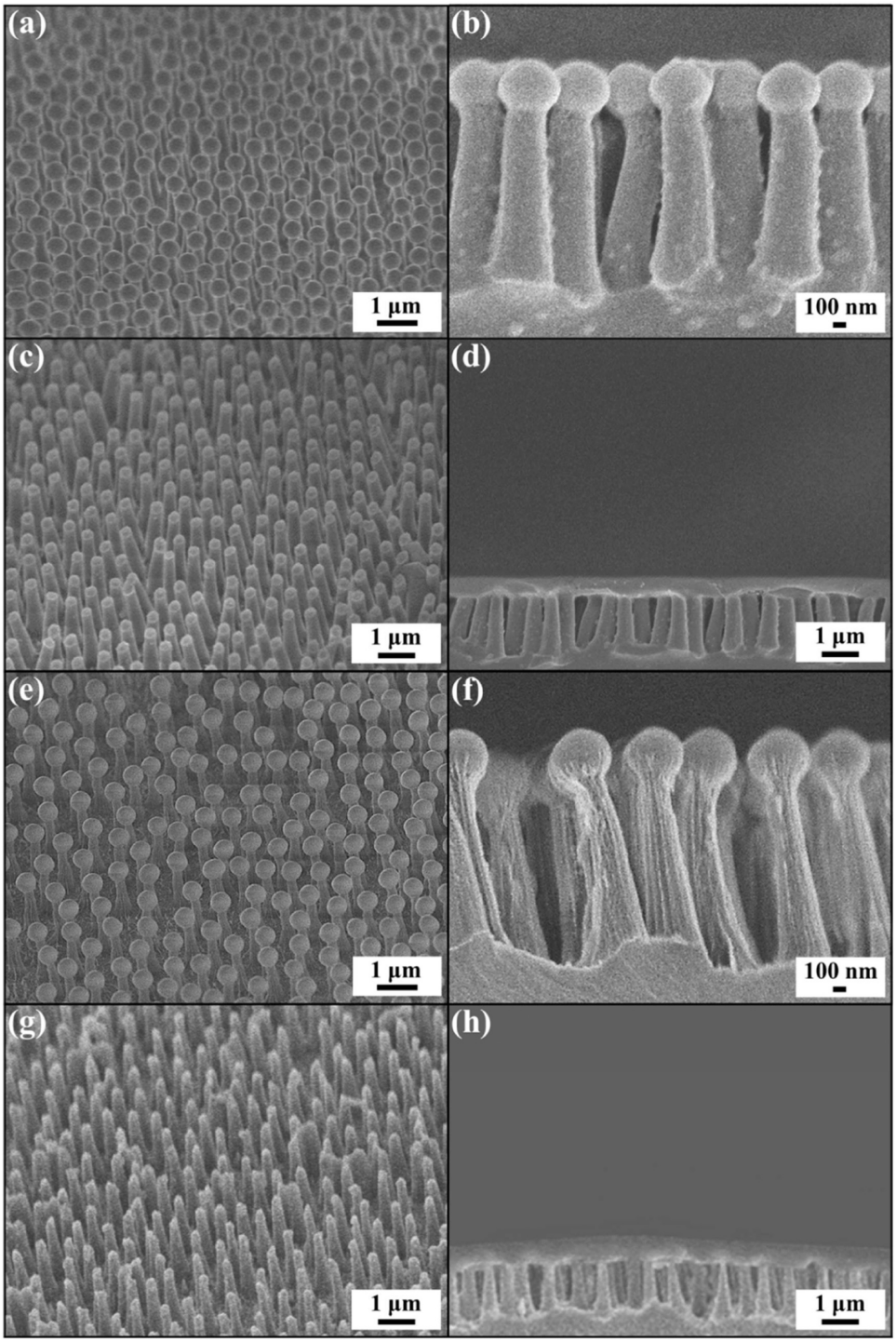

Figure 7. (a) Tilted-view SEM image and (b) magnified cross-sectional SEM image of the king oyster mushroom-like structure array templated from a nonclose-packed colloidal monolayer of 500 nm silica spheres by reactive ion etching (Ar/O_2 (10 SCCM/15 SCCM)). The average interparticle distance is controlled to be 1.4 *D*, where *D* denotes the diameter of silica spheres. (c) Tilted-view SEM image of the corresponding frustum-shaped structure array. (d) Cross-sectional SEM image of the as-fabricated impact-resistant structures. (e) Tilted-view SEM image and (f) magnified cross-sectional SEM image of the king oyster mushroom-like structure array templated from the nonclose-packed silica colloidal crystals by reactive ion etching (Ar/O_2 (10 SCCM/30 SCCM)). (g) Tilted-view SEM image of the corresponding cone-shaped structure array. (h) Cross-sectional SEM image of the as-fabricated impact-resistant structures.

coating layer is controlled to be 500 nm, 1 μm, and 500 nm, respectively. On the other hand, the sandwich structure is comprised of a 500 nm-thick PETPTA/PEGDA (20:1) upper layer, a 1 μm-high PETPTA/PEGDA (1:3) column-shaped structure array, and a 500 nm-thick PETPTA/PEGDA (20:1) lower layer. These structural supports are templated from nonclose-packed 500 nm silica colloidal crystals (1.4 *D*). As one would expect, the application of larger loads (500 μN) causes both specimens to be deformed more seriously, thereby dissipating much more impact energies. It is evident that the

https://doi.org/10.1021/acsami.5c03894
ACS Appl. Mater. Interfaces 2025, 17, 24630−24643

Table 4. Values of Young's Modulus, Hardness, and Dissipation Energy for the Taiwan Rhinoceros Beetle-Inspired Impact-Resistant Structures with Varied Structure Shapes[1]

Sample	Porosity	Experimental / Theorical Young's Modulus (GPa)	Hardness (GPa)	Dissipation Energy (10^{-12} J)
Column	0.27	2.50 ± 0.22 / 2.62	0.08 ± 0.01	9.31 ± 0.15
Frustum	0.31	2.13 ± 0.07 / 2.46	0.07 ± 0.01	9.61 ± 0.41
Cone	0.35	1.50 ± 0.14 / 2.33	0.06 ± 0.01	12.71 ± 1.04

[1]The inter-structure distances are adjusted to be 1.4 *D*, where *D* denotes the diameter of silica spheres (500 nm).

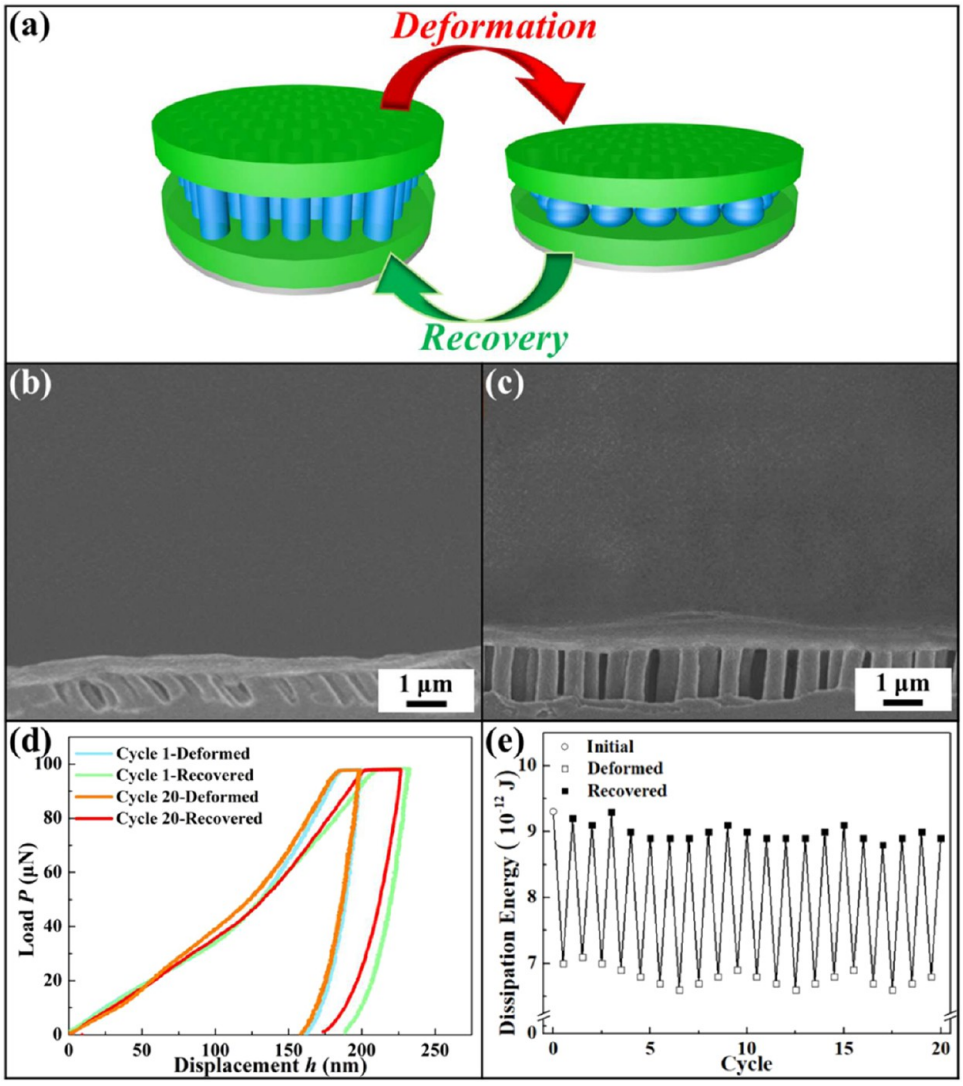

Figure 8. (a) Illustration of the reversibly recoverable Taiwan rhinoceros beetle-inspired impact-resistant structures. Cross-sectional SEM images of the (b) deformed and (c) recovered impact-resistant structures. The impact-resistant structures are templated from nonclose-packed 500 nm silica colloidal crystals by reactive ion etching (Ar (40 SCCM)). The interstructure distance is controlled to be 1.4 *D*, where *D* denotes the diameter of silica spheres. (d) Load−displacement curves with maximum loads of 100 μN for the temporarily deformed and recovered impact-resistant structures after the 1st and 20th deformation/recovery cycles. (e) Values of dissipation energy for the temporarily deformed and recovered impact-resistant structures after 20 deformation/recovery cycles.

https://doi.org/10.1021/acsami.5c03894
ACS Appl. Mater. Interfaces 2025, 17, 24630−24643

evaluated dissipation energy of the triple-layer PETPTA/PEGDA coating is considerably increased from 5.71 ± 0.14 to 120.83 ± 7.10 pJ once the maximum load changes from 100 to 500 μN (Table S3). In comparison, a dissipation energy of 173.48 ± 10.86 pJ can be achieved as a load of 500 μN is applied to the bioinspired sandwich structures. The results reveal that the impact-resistant capability of sandwich structures can even be enhanced under larger loads.

Critically, the PETPTA/PEGDA (1:3) behaves with room-temperature shape memory characteristics, which enable structural transitions between temporarily deformed and permanent states in response to external stimuli under ambient conditions (Figure 8(a)). As displayed in Figure 8(b), the PETPTA/PEGDA (1:3) column-shaped structural supports are distorted in shape dramatically once the bioinspired sandwich structure is physically compressed by the nanoindenter tip with a maximum load of 100 μN. The structural deformation assuredly brings about a reduction in porosity within this squeezed sandwich structure and a diminished impact-resistant capability. Beyond that, the appearance of the deformed structure-coated glass substrate turns into a whitish color due to the light scattering from deformed structures (Figure S15). Importantly, these temporarily deformed structural supports can recover their permanent configurations in a few seconds by drying out of low-surface-tension liquids, such as ethanol, at room temperature. After being rinsed with ethanol, the PETPTA/PEGDA (1:3) network undergoes a substantial swelling, which relaxes the stretched copolymer chains and enhances their mobilities. The contorted sandwich structure, therefore, gradually reverts to its original conformation by an evaporation-induced capillary force during ethanol evaporation (Figure 8(c)). The resulting shape recovery further allows the sandwich structure to restore its inherent appearance and impact resistance. As verified in Figure 8(d) and Table S4, the corresponding dissipation energy has been increased from 6.99 ± 0.25 to 9.05 ± 0.25 pJ, which is even consistent with that of an undeformed sandwich structure (9.31 ± 0.15 pJ). Although the restored impact-resistant capabilities are slightly reduced over 20 deformation/recovery cycles (Figure 8 (d),(e)), it is validated that the sandwich structure can be reversibly deformed and recovered through drying out of ethanol. To put it simply, the presence of shape memory polymer-based structural supports provides a facile strategy to realize recoverable impact-resistant structures (Figure S16). In sharp contrast, the impact resistance of the sandwich structure supported by frustum-shaped structural supports is diminished significantly after a few deformation/recovery cycles (Figure S17). Despite the fact that those frustum-shaped structures can be deformed more easily to dissipate more impact energies, it is found that the highly impaired sandwich structure cannot be fully recovered, which greatly impedes its ultimate performance and practical applications.

CONCLUSIONS

To conclude, Taiwan rhinoceros beetle-inspired sandwich structures, supported by nonclose-packed shape memory polymer-based structure arrays, have been engineered by integrating a scalable colloidal self-assembly methodology and a colloidal lithographic approach. Upon applying external stresses onto the bioinspired sandwich structures, the structural supports can be contorted easily to dissipate impact energies effectively. In addition, it is evidenced that the introduction of larger porosity within the sandwich structure brings about a reduced Young's modulus, allowing the structure to dissipate impact energy more efficiently. Critically, these temporarily deformed structural supports can further recover their permanent shapes through drying out of ethanol, and the corresponding impact resistance is therefore restored. Although the size of spin-coating equipment still restricts the scale of the as-engineered impact-resistant structures, the stimuli-responsive structural transitions associated with the reversibly recoverable impact-resistant capabilities undoubtedly create novel dimensions for a range of practical applications in miniaturized devices.

ASSOCIATED CONTENT

Supporting Information

The Supporting Information is available free of charge at https://pubs.acs.org/doi/10.1021/acsami.5c03894.

Porosities, Young's moduli, hardnesses, and dissipation energies of a Taiwan rhinoceros beetle and the Taiwan rhinoceros beetle-inspired impact-resistant structures. Schematic illustration of the templating procedures for engineering the bioinspired impact-resistant structures with varied structural configurations. Photographic images, surface morphologies, and load−displacement curves of featureless copolymer layer-coated glass substrates and the glass substrates coated with bioinspired impact-resistant structures with varied structural configurations (PDF)

AUTHOR INFORMATION

Corresponding Author

Hongta Yang − *Department of Chemical Engineering, National Chung Hsing University, Taichung 40227, Taiwan;* orcid.org/0000-0002-5822-1469; Email: hyang@dragon.nchu.edu.tw

Authors

Mei-Xuan Wu − *Department of Chemical Engineering, National Chung Hsing University, Taichung 40227, Taiwan*

Hsiang-Wen Hsueh − *Department of Chemical Engineering, National Chung Hsing University, Taichung 40227, Taiwan*

Shang-Hsuan Lu − *Department of Chemical Engineering, National Chung Hsing University, Taichung 40227, Taiwan*

Bo-Han Zeng − *Department of Chemical Engineering, National Chung Hsing University, Taichung 40227, Taiwan*

Yun-Wen Huang − *Department of Chemical Engineering, National Chung Hsing University, Taichung 40227, Taiwan*

Cai-Yin Fang − *Department of Chemical Engineering, National Chung Hsing University, Taichung 40227, Taiwan*

Szu-Yi Yeh − *Department of Chemical Engineering, National Chung Hsing University, Taichung 40227, Taiwan*

Shih-Hsuan Hsieh − *Department of Chemical Engineering, National Chung Hsing University, Taichung 40227, Taiwan*

Complete contact information is available at: https://pubs.acs.org/10.1021/acsami.5c03894

Author Contributions

†M.-X.W. and H.-W.H. contributed equally to this work.

Notes

The authors declare no competing financial interest.

ACKNOWLEDGMENTS

The National Science and Technology of Council (NSTC 112-2221-E-005-006-MY3) and the Innovative Center on Sustain-

able Negative-Carbon Resources under the Ministry of Education are acknowledged for the financial support.

REFERENCES

(1) Park, S. Y.; Lee, S.; Yang, J.; Kang, M. S. Patterning Quantum Dots via Photolithography: A Review. *Adv. Mater.* **2023**, *35* (41), No. 2300546.
(2) Reda, A.; El-Safty, S. A.; Selim, M. M.; Shenashen, M. A. Optical Glucose Biosensor Built-in Disposable Strips and Wearable Electronic Devices. *Biosens. Bioelectron.* **2021**, *185*, No. 113237.
(3) Liu, Z.; Zhang, S.; Wu, Z.; Mu, E.; Wei, H.; Liu, Y.; Shi, H.; Hu, Z. High-Performance Integrated Chip-Level Thermoelectric Device for Power Generation and Microflow Detection. *Nano Energy* **2023**, *114*, No. 108611.
(4) Zhang, W.; Luo, Y.; Tao, J.; Liu, G.; Li, B.; Teng, Y.; Xu, J.; Feng, L.; You, Z. Miniaturized and Portable Device for Noninvasive, Ultrasensitive and Point-of-Care Diagnosis by Engineered Metal-Carbide-Based Field Effect Transistor. *J. Chem. Eng.* **2025**, *506*, No. 160264.
(5) Gangwar, R.; Pathak, A.; Chiavaioli, F.; Bakar, M. A.; Kamil, Y.; Mahdi, M.; Singh, V. Optical fiber SERS sensors: Unveiling Advances, Challenges, and Applications in a Miniaturized Technology. *Coord. Chem. Rev.* **2024**, *510*, No. 215861.
(6) Wang, B.; Li, G.; Xu, L.; Liao, J.; Zhang, X. Nanoporous Boron Nitride Aerogel Film and Its Smart Composite with Phase Change Materials. *ACS Nano* **2020**, *14* (12), 16590−16599.
(7) Yin, Y.; Chen, H.; Deng, G.; Su, L.; Wu, W.; Yan, M.; Dong, Y.; Xu, X.; Deng, Z.; Tan, Q.; et al. A Self-Optimized Alloy With Multi-Scale Hierarchical Microstructure and Enhanced Mechanical Properties. *Mater. Des.* **2025**, *250*, No. 113620.
(8) Xiang, Z.; Yang, Q.; Zhang, T.; Shen, X.; Hao, S.; Chen, J.; Huang, S. Tensile Mechanical Behavior of Functionally Graded NiTi Alloy Manufactured via Laser Powder Bed Fusion. *Mater. Sci. Eng., A* **2024**, *914*, No. 147119.
(9) de Araujo, A. P.; Pauly, S.; Batalha, R. L.; Coury, F. G.; Kiminami, C. S.; Uhlenwinkel, V.; Gargarella, P. Additive Manufacturing of a Quasicrystal-Forming $Al_{95}Fe_2Cr_2Ti_1$ Alloy with Remarkable High-Temperature Strength and Ductility. *Addit. Manuf.* **2021**, *41*, No. 101960.
(10) Sellappan, P.; Wang, E.; Santos, C. J. E.; On, T.; Lambros, J.; Kriven, W. M. Wave Propagation Through Alumina-Porous Alumina Laminates. *J. Eur. Ceram. Soc.* **2015**, *35* (1), 197−210.
(11) Shadman, M.; Ziari, H. Laboratory Evaluation of Fatigue Life Characteristics of Polymer Modified Porous Asphalt: A Dissipated Energy Approach. *Constr. Build. Mater.* **2017**, *138*, 434−440.
(12) Sun, Z.; Murugaiah, A.; Zhen, T.; Zhou, A.; Barsoum, M. Microstructure and Mechanical Properties of Porous Ti_3SiC_2. *Acta. Mater.* **2005**, *53* (16), 4359−4366.
(13) Lazarus, B. S.; Velasco-Hogan, A.; Río, T. G.-d.; Meyers, M. A.; Jasiuk, I. A Review of Impact Resistant Biological and Bioinspired Materials and Structures. *J. Mater. Res. Technol.* **2020**, *9* (6), 15705−15738.
(14) Peyrton, J.; Avérous, L. Structure-Properties Relationships of Cellular Materials from Biobased Polyurethane Foams. *Mater. Sci. Eng., R* **2021**, *145*, No. 100608.
(15) McKenna, D. D.; Shin, S.; Ahrens, D.; Balke, M.; Beza-Beza, C.; Clarke, D. J.; Donath, A.; Escalona, H. E.; Friedrich, F.; Letsch, H.; et al. The Evolution and Genomic Basis of Beetle Diversity. *Proc. Natl. Acad. Sci. U.S.A.* **2019**, *116* (49), 24729−24737.
(16) Chen, J. X.; Xie, J.; Wu, Z. S.; Elbashiry, E. M. A.; Lu, Y. Review of Beetle Forewing Structures and Their Biomimetic Applications in China: (I) On the Structural Colors and the Vertical and Horizontal Cross-Sectional Structures. *Mater. Sci. Eng., C* **2015**, *55*, 605−619.
(17) Dale, C. Evolution: Weevils Get Tough on Symbiotic Tyrosine. *Curr. Biol.* **2017**, *27* (23), R1282−R1284.
(18) Fang, J. W.; Li, Z. P.; Chen, C.; Fan, B. An Low-Frequency Vibration Isolation Structure Inspired by Ladybird Sheath. *Int. J. Mech. Sci.* **2025**, *286*, No. 109906.
(19) Chen, J. X.; Wu, G. Beetle forewings: Epitome of the Optimal Design for Lightweight Composite Materials. *Carbohydr. Polym.* **2013**, *91* (2), 659−665.
(20) Duan, Y.; Zhang, T.; Zhou, J.; Xiao, H.; Chen, X.; Al Teneiji, M.; Guan, Z. W.; Cantwell, W. J. Energy-Absorbing Characteristics of Hollow-Cylindrical Hierarchical Honeycomb Composite Tubes Inspired a Beetle Forewing. *Compos. Struct.* **2021**, *278*, No. 114637.
(21) Del Sol, J. F.; Hongo, Y.; Boisseau, R. P.; Berman, G. H.; Allen, C. E.; Emlen, D. J. Population Differences in the Strength of Sexual Selection Match Relative Weapon Size in the Japanese Rhinoceros Beetle,Trypoxylus Dichotomus(Coleoptera: Scarabaeidae). *Evolution* **2021**, *75* (2), 394−413.
(22) Murata, S.; Rivera, J.; Noh, M. Y.; Hiyoshi, N.; Yang, W.; Parkinson, D. Y.; Barnard, H. S.; Arakane, Y.; Kisailus, D.; Arakaki, A. Unveiling Characteristic Proteins for the Structural Development of Beetle Elytra. *Acta Biomater.* **2022**, *140*, 467−480.
(23) Chen, J. X.; Xie, J.; Zhu, H.; Guan, S. J.; Wu, G.; Noori, M. N.; Guo, S. J. Integrated Honeycomb Structure of a Beetle Forewing and Its Imitation. *Mater. Sci. Eng., C* **2012**, *32* (3), 613−618.
(24) Liu, B.; Xu, X. H. Study on Impact Resistance of Bionic Interlocking Brick-Mud Structures. *Compos. Struct.* **2023**, *318*, No. 117103.
(25) Rivera, J.; Murata, S.; Hosseini, M. S.; Trikanad, A. A.; James, R.; Pickle, A.; Yaraghi, N.; Matsumoto, N.; Yang, W.; Parkinson, D. Y.; et al. Structural Design Variations in Beetle Elytra. *Adv. Funct. Mater.* **2021**, *31* (50), No. 2106468.
(26) Tan, A. T. L.; Nagelberg, S.; Chang-Davidson, E.; Tan, J.; Yang, J. K. W.; Kolle, M.; Hart, A. J. In-Plane Direct-Write Assembly of Iridescent Colloidal Crystals. *Small Struct.* **2020**, *16* (4), No. 1905519.
(27) Tzadka, S.; Martin, C. U.; Toledo, E.; Yassin, A. A. K.; Pandey, A.; Le Saux, G.; Porgador, A.; Schvartzman, M. A Novel Approach for Colloidal Lithography: From Dry Particle Assembly to High-Throughput Nanofabrication. *ACS Appl. Mater. Interfaces* **2024**, *16* (14), 17846−17856.
(28) Keller, A. W.; Marino, E.; An, D.; Neuhaus, S. J.; Elbert, K. C.; Murray, C. B.; Kagan, C. R. Sub-5 nm Anisotropic Pattern Transfer via Colloidal Lithography of a Self-Assembled GdF_3 Nanocrystal Monolayer. *Nano Lett.* **2022**, *22* (5), 1992−2000.
(29) Wang, Y.; Xu, Z.; Zhao, S.; Zhang, Y.; Li, W.; Wen, J.; Gao, R.; Zheng, B.; Liang, L.; Zhao, X. Anisotropic Growth of Ag Nanonails Induced by Plasmon-Mediated Chemical Reactions in Cross-Shaped Nanocavity Array. *Colloids Surf., A* **2024**, *703*, No. 135189.
(30) Lotito, V.; Zambelli, T. Playing with Sizes and Shapes of Colloidal Particles via Dry Etching Methods. *Adv. Colloid Interface Sci.* **2022**, *299*, No. 102538.
(31) Ding, X.; Rubby, M. F.; Que, S.; Uchayash, S.; Que, L. Facile Process for Fabrication of Silicon Micro−Nanostructures of Different Shapes as Molds for Fabricating Flexible Micro−Nanostructures and Wearable Sensors. *ACS Appl. Mater. Interfaces* **2023**, *15* (9), 12202−12208.
(32) Chen, Y.-J.; Fang, C.-Y.; Huang, Y.-W.; Hsu, T.-F.; Tang, N.-T.; Tsai, H.-P.; Lee, R.-H.; Lin, S.-H.; Hsuen, H.-W.; Lin, K.-Y. A.; Yang, H. White Roman Goose Feather-Inspired Unidirectionally Inclined Conical Structure Arrays for Switchable Anisotropic Self-Cleaning. *ACS Appl. Mater. Interfaces* **2024**, *16* (28), 36840−36850.
(33) Fang, X.; Zheng, C.; Yin, Z.; Wang, Z.; Wang, J.; Liu, J.; Luo, D.; Liu, Y. J. Hierarchically Ordered Silicon Metastructures from Improved Self-Assembly-Based Nanosphere Lithography. *ACS Appl. Mater. Interfaces* **2020**, *12* (10), 12345−12352.
(34) Jiang, P.; Prasad, T.; McFarland, M. J.; Colvin, V. L. Two-Dimensional Nonclose-Packed Colloidal Crystals Formed by Spincoating. *Appl. Phys. Lett.* **2006**, *89* (1), No. 011908.
(35) Jiang, P.; McFarland, M. J. Wafer-Scale Periodic Nanohole Arrays Templated from Two-Dimensional Nonclose-Packed Colloidal Crystals. *J. Am. Chem. Soc.* **2005**, *127* (11), 3710−3711.
(36) Luo, L.; Zhang, F.; Wang, L.; Liu, Y.; Leng, J. Recent Advances in Shape Memory Polymers: Multifunctional Materials, Multiscale Structures, and Applications. *Adv. Funct. Mater.* **2024**, *34* (14), No. 2312036.

https://doi.org/10.1021/acsami.5c03894
ACS Appl. Mater. Interfaces 2025, 17, 24630−24643

(37) Sun, L.; Gao, X.; Wu, D.; Guo, Q. Advances in Physiologically Relevant Actuation of Shape Memory Polymers for Biomedical Applications. *Polym. Rev.* **2021**, *61* (2), 280−318.
(38) Ganewatta, M. S.; Wang, Z.; Tang, C. Chemical Syntheses of Bioinspired and Biomimetic Polymers Toward Biobased Materials. *Nat. Rev. Chem.* **2021**, *5* (11), 753−772.
(39) Zheng, N.; Xu, Y.; Zhao, Q.; Xie, T. Dynamic Covalent Polymer Networks: A Molecular Platform for Designing Functions beyond Chemical Recycling and Self-Healing. *Chem. Rev.* **2021**, *121* (3), 1716−1745.
(40) Xia, Y.; He, Y.; Zhang, F.; Liu, Y.; Leng, J. A Review of Shape Memory Polymers and Composites: Mechanisms, Materials, and Applications. *Adv. Mater.* **2021**, *33* (6), No. 2000713.
(41) Wijerathne, B.; Liao, T.; Ostrikov, K.; Sun, Z. Bioinspired Robust Mechanical Properties for Advanced Materials. *Small Struct.* **2022**, *3* (9), No. 2100228.
(42) Stöber, W.; Fink, A.; Bohn, E. Controlled Growth of Monodisperse Silica Spheres in the Micron Size Range. *J. Colloid Interface Sci.* **1968**, *26* (1), 62−69.
(43) Jiang, P.; McFarland, M. J. Large-Scale Fabrication of Wafer-Size Colloidal Crystals, Macroporous Polymers and Nanocomposites by Spin-Coating. *J. Am. Chem. Soc.* **2004**, *126* (42), 13778−13786.
(44) Leverant, C. J.; Leo, S.-Y.; Cordoba, M. A.; Zhang, Y.; Charpota, N.; Taylor, C.; Jiang, P. Reconfigurable Anticounterfeiting Coatings Enabled by Macroporous Shape Memory Polymers. *ACS Appl. Polym. Mater.* **2019**, *1* (1), 36−46.
(45) Islam, M. T.; Tang, S.; Liverani, C.; Saha, S.; Tasciotti, E.; Righetti, R. Non-Invasive Imaging of Young's Modulus and Poisson's Ratio in Cancers in Vivo. *Sci. Rep.* **2020**, *10* (1), No. 7266.
(46) Li, W.; Wang, M.; Cheng, J. Indentation Hardness of the Cohesive-Frictional Materials. *Int. J. Mech. Sci.* **2020**, *180*, No. 105666.
(47) Dong, J. L.; Li, F. C.; Gu, Z. P.; Jiang, M. Q.; Liu, Y. H.; Wang, G. J.; Wu, X. Q. Impact Resistance and Energy Dissipation Mechanism of Nanocrystalline CoCrNi Medium Entropy Alloy Nanofilm under Supersonic Micro-Ballistic Impact. *Int. J. Plast.* **2023**, *171*, No. 103801.
(48) Dai, Z.; Yang, Z. Macro-/Micro-Structures of Elytra,Mechanical Properties of the Biomaterial and the Coupling Strength between Elytra in Beetles. *J. Bionic Eng.* **2010**, *7* (1), 6−12.
(49) Kováčik, J. Correlation between Elastic Modulus, Shear Modulus, Poisson's Ratio and Porosity in Porous Materials. *Adv. Eng. Mater.* **2008**, *10* (3), 250−252.
(50) Jiang, Z.; Chen, N.; Yi, Z.; Zhong, J.; Zhang, F.; Ji, S.; Liao, R.; Wang, Y.; Li, H.; Liu, Z.; et al. A 1.3-Micrometre-Thick Elastic Conductor for Seamless on-Skin and Implantable Sensors. *Nat. Electron.* **2022**, *5* (11), 784−793.
(51) Jiang, P.; Bertone, J.; Hwang, K. S.; Colvin, V. Single-Crystal Colloidal Multilayers of Controlled Thickness. *Chem. Mater.* **1999**, *11* (8), 2132−2140.
(52) Fang, Y.; Leo, S.-Y.; Ni, Y.; Wang, J.; Wang, B.; Yu, L.; Dong, Z.; Dai, Y.; Basile, V.; Taylor, C.; Jiang, P. Reconfigurable Photonic Crystals Enabled by Multistimuli-Responsive Shape Memory Polymers Possessing Room Temperature Shape Processability. *ACS Appl. Mater. Interfaces* **2017**, *9* (6), 5457−5467.
(53) Fang, Y.; Ni, Y.; Leo, S.-Y.; Taylor, C.; Basile, V.; Jiang, P. Reconfigurable Photonic Crystals Enabled by Pressure-Responsive Shape-Memory Polymers. *Nat. Commun.* **2015**, *6* (1), No. 7416.
(54) Hertz, H. *Miscellaneous Papers*; Macmillan and Co., Ltd.: New York, 1896.
(55) Kurosaki, K.; Saito, Y.; Muta, H.; Uno, M.; Yamanaka, S. Nanoindentation Studies of UO_2 and (U, Ce) O_2. *J. Alloys Compd.* **2004**, *381* (1−2), 240−244.
(56) Gaillard, Y.; Jimenez-Piqué, E.; Oliva-Ramirez, M.; Rico, V. J.; Gonzalez-Elipe, A. R. Extraction of Microstructural Parameters from Sculptured Thin Films Nanoindentation. *Surf. Coat. Technol.* **2021**, *425*, No. 127696.

https://doi.org/10.1021/acsami.5c03894
ACS Appl. Mater. Interfaces 2025, 17, 24630−24643